Supporting Information for

Stable and efficient single-atom Zn catalyst for CO_2 reduction to CH_4

Lili Han[†‡1], Shoujie Song[†1], Mingjie Liu[‖1], Siyu Yao[§], Zhixiu Liang[§], Hao Cheng[‡], Zhouhong Ren[†], Wei Liu[†], Ruoqian Lin[§], Gaocan Qi[⊥], Xijun Liu*[†], Qin Wu*[‖], Jun Luo*[†], and Huolin L. Xin*[‡]

[†] Center for Electron Microscopy and Tianjin Key Lab of Advanced Functional Porous Materials, Institute for New Energy Materials & Low-Carbon Technologies, School of Materials Science and Engineering, Tianjin University of Technology, Tianjin 300384, China

[‡] Department of Physics and Astronomy, University of California, Irvine, CA 92697, USA

[‖] Center for Functional Nanomaterials, Brookhaven National Laboratory, Upton, NY 11973, USA

[§] Chemistry Division, Brookhaven National Laboratory, Upton, NY 11973, USA

[⊥] School of Materials Science and Engineering, Tianjin University of Technology, Tianjin 300384, China

This PDF file includes:

1. Experimental Section

Synthesis of SA-Zn/MNC

SA-Zn/MNC was synthesized by a dissolution-and-carbonization method. In details, 144 mg anhydrous glucose ($C_6H_{12}O_6$), 192.6 mg zinc acetate dihydrate ($C_4H_6O_4Zn{\cdot}2H_2O$) and 690 mg hydroxylammonium chloride ($(NH_3OH)Cl$) were ultrasonically dissolved in 80 mL of deionized water-ethanol solution (with a volume ratio of 1:1) to form a transparent solution. The solution was placed in a drying oven at 70 ℃ to evaporate water and ethanol, and the obtained solid was ground into powder. The precursor powder was placed in a crucible, heated in a tube furnace to 800 °C with a rate of 5 °C min^{-1} and carbonized at 800 °C for 4 h under Ar protection atmosphere. The obtained black product was ground into fine powder and denoted as SA-Zn/MNC. For comparison, the catalysts with Zn loadings of 0.95 wt%, 1.56 wt%, 2.07 wt%, and 3.05 wt% were synthesized with zinc acetate dihydrate masses of 69.2 mg, 113.5 mg, 150.8 mg, and 221.9 mg, respectively, according to the synthetic procedures above. The MNC sample without Zn was synthesized under the same conditions as SA-Zn/MNC except that no $C_4H_6O_4Zn{\cdot}2H_2O$ was added.

Characterizations

XRD patterns were collected using an X-ray diffractometer (Rigaku D/max 2500) at a scan rate of 10 ° min^{-1} in the 2θ range of 10 – 90 °. SEM observations were performed using a field-emission-gun (FEG) SEM instrument (Verios 460L of FEI). TEM images and SAED patterns were achieved using an FEI Talos F200X S/TEM with an FEG. Atomic-resolution HAADF-STEM images and EDS mappings were taken using an FEI Titan Cubed Themis G2 300 S/TEM with a probe corrector. Hard XAS measurements were carried out at Beamline 8-ID, National Synchrotron Light Source II, Brookhaven National Laboratory. Zn K-edge absorption spectra were acquired using a cryogenically cooled double crystal Si (1111) monochromator. The spectra were recorded in the fluorescence mode with a passivated implanted planar silicon (PIPS) detector. XPS experiments were carried out on a Kratos AXIS Ultra DLD system with Al Kα radiation as the X-ray source. Nitrogen adsorption and desorption isotherms were measured at 77 K with an Autosorb-iQ-MP Micromeritics analyzer. Raman spectroscopy was obtained using high-resolution confocal micro-Raman spectrometer with the model of HORIBA EVOLUTION.

CO_2 electrochemical measurements

The electrochemical measurements were conducted at 25 °C by an electrochemical workstation (CHI 760E) in a two-compartment batch cell containing 20 mL of 1 M $KHCO_3$ solution. A platinum foil and a saturated calomel electrode (SCE) were employed as the counter and the reference electrodes, respectively. For the preparation of a working electrode, 10 mg sample and 40 μL Nafion solution (5 wt%) were dispersed in 1

mL water-ethanol solution with a volume ratio of 3:1. The dispersion was ultrasonicated for 1 h to form a homogeneous ink. Then, 40 μL of the ink was coated onto a carbon fiber cloth (1 cm × 1 cm) to prepare a working electrode. All current density values were normalized by the geometric area of the electrode. Before the electrochemical CO_2 reduction test, a flow high-purity CO_2 with a flow rate of 200 sccm (standard cubic centimeter per minute) was purged into the 20 mL 1 M $KHCO_3$ for 30 min to remove air in the solution and ensure to reach saturation. After that, the flow rate of CO_2 was adjusted as 20 sccm for the electrolysis. During the ERC test process, *i*R drop compensation was performed using the CHI 760E software. Cyclic voltammetry (CV) measurement was first performed at least 50 cycles with a scan rate of 10 mV s^{-1} between −2 V and 0 V vs. SCE. LSV measurements were carried out to examine the sample's electrochemical activity with a scan rate of 10 mV s^{-1} in the voltage range between –2 and 0 V vs. SCE. Electrolysis experiments were conducted using the chronoamperometry method at the selected potential for 120 min. A gas chromatograph (GC, Agilent 7890A) and a ^1H nuclear magnetic resonance (NMR, Bruker NMR400) spectroscopy were used to detect the gaseous products of CO_2 reduction after the electrolysis. The amounts of the ERC reduction products were calculated according to the external standard method. Tafel slopes for CH_4 production were calculated via stepped-potential electrolysis experiments, where partial current densities for CH_4 production were calculated from the GC graph of CH_4 product after electrolysis for 2h.

For the ^{13}C-labeled isotope experiment, isotopic $^{13}CO_2$ with a purity level of 99.9% was purchased from Cambridge Isotope Laboratories. Electrolysis was conducted in $^{13}CO_2$ purged acetonitrile for two hours at −1.8 V vs. SCE and the gas products were carefully transferred to evacuated 20 mL cramp-type headspace vial through a needle. Gas chromatography-mass spectrometry (GC-MS, Agilent, 7890A GC/5977A MS) with a quadrupole-type mass spectrometer and HP-PLOT molesieve capillary column (Agilent) was used for the measurements of the mass of the products. 100 μL of the gas was injected into the GC-MS by a syringe. The mass of products was analyzed after segregation by a gas chromatograph.

The calculation method for Faradaic efficiency

The FEs of the gas products were calculated by using the following equation:

$$FE_{gas}\ (\%) = (C_{gas} \times V_{CO2} \times 10^{-3} \times t \times F \times N)/1344Q$$

where C_{gas} is the concentration of the gas-phase products, based on calibration of the GC; V_{CO2} is the flow rate of CO_2 (= 20 sccm); t is electrolysis (= 120 min); F is the Faraday constant (96485 C mol^{-1}); N is the number of transferred electrons for gas-phase products; Q (C) is the total quantity of electric charge.

The liquid products were analyzed through nuclear magnetic resonance (NMR, AVANCE AV III 400 Bruker, Germany), in which 0.5 mL electrolyte containing the obtained liquid-phase products was mixed with 0.1 mL D_2O and 0.03 μL dimethyl sulfoxide (DMSO), where DMSO was used as an internal standard to quantify and calibrate the liquid product. The ^1H spectrum was measured with water suppression via a presaturation method. The FE of liquid-phase products were calculated as follows:

$$FE_{liquid}\ (\%) = (n \times F \times N)/Q$$

where n (mol) is the content of the liquid-phase products, based on the calibration of the NMR; N is the number of transferred electrons for liquid-phase products; F is the Faraday constant (96485 C mol^{-1}); Q (C) is the total quantity of electric charge.

Operando ATR-SEIRAS experiment

A Nicolet iS50 FTIR spectrometer equipped with a mercury cadmium telluride (MCT) detector cooled with liquid nitrogen was employed for the electrochemical ATR-SEIRAS measurements in a CO_2-saturated 1 M $KHCO_3$ solution. All spectra are given in absorbance and defined as $A=-\log(R/R_{ref})$, where R and R_{ref} represent the reflected intensity of the sample and reference single beam spectrum, respectively. Reference spectra were taken at 0 V vs. RHE. Three-electrode configuration was utilized for electrochemical control. A double-bridged Ag/AgCl electrode and Pt foil served as the reference and the counter electrodes, respectively. The working electrode was fabricated by drop-casting catalysts onto underlayer Au film on Si ATR hemisphere with a loading of 10 μg cm^{-2}. Detailed procedures on the Au underlayer preparation can be found in a previously reported protocol of electroless Au deposition.[S1] Real-time spectra were collected at a resolution of 4 cm^{-1}, and each spectrum was integrated by 288 scans.

DFT Calculations

The DFT calculations were performed with VASP.[S2] The PBE functional[S3] with projector augmented wave (PAW) method [S4] is used. The modeled graphene supercell is 5×5 with one Zn-N_4 motif and a 15 Å vacuum layer. The K point mesh is $3\times3\times1$. The kinetic energy cutoff is 450 eV in plane-wave basis. Spin-polarization is included. For each step, possible configurations are generated and relaxed with the force convergence < 0.05 eV $Å^{-1}$. The configurations with the lowest energies are identified as the most stable structures. The free energies of adsorbates are calculated as $\Delta G=\Delta E_{ele}+E_{ZPE}-TS_{vib}$. The zero-point vibration (ZPE) is calculated under the harmonic oscillator approximation with the fixed substrate. The vibrational entropy is $S_{vib} = \sum_{\varepsilon_i}[\frac{\beta\varepsilon_i}{\exp(\beta\varepsilon_i)-1} - \ln[1-\exp(-\beta\varepsilon_i)]]$, where ε_i is the vibrational energy of each mode. The proton and the electron are assumed to be coupled for each reduction step. The Computational Hydrogen Electrode (CHE) model is used to calculate the chemical potential of proton-electron pair.[S5] For

non-adsorbed molecules (CO_2, CH_4, H_2), the E_{ele} and E_{ZPE} are calculated from DFT and the entropies are used as the standard entropy under 298.15 K from the NIST webbook.[S6] The H_2O entropy is used under the vapor pressure of 298.15 K. The solvation corrections are taken from ref. S5, in which *OH, *CHO, *OCHOH (*COOH) and *CHO are stabilized by 0.5 eV, 0.1 eV, 0.25 eV and 0.05 eV, respectively.

For the intermediate *OCH a molecular analogue of the catalyst[S7] (Scheme S1) is also used to probe the energy of the adsorbed anion. Calculations are done using Gaussian 16[S8] with the same PBE functional and 6-31G(d) basis set for all atoms except Zn, which has the LANL2DZ effective core potential and its associated basis set. Both adsorbed *OCH and its anion $*OCH^-$ are fully relaxed. The results are that $*OCH^-$ is lower in energy than *OCH by 1.4 eV, a very significant energy drop. It thus strongly suggests that $*OCH^-$ can be a potential intermediate step, resulting from transfer of two electrons and one proton to the step 2 intermediate *OCHOH. $*OCH^-$ will turn into the step 4 intermediate $*OCH_2$ with another proton transfer. In this case, the *CHO intermediate is avoided, and the kinetics from Step 2 to Step 4 are much simpler without any binding-site change.

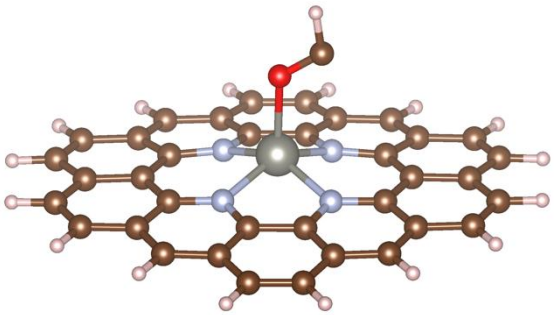

Scheme S1. Adsorbed *OCH on a molecular analogue of the catalyst.

2. Figures and Tables

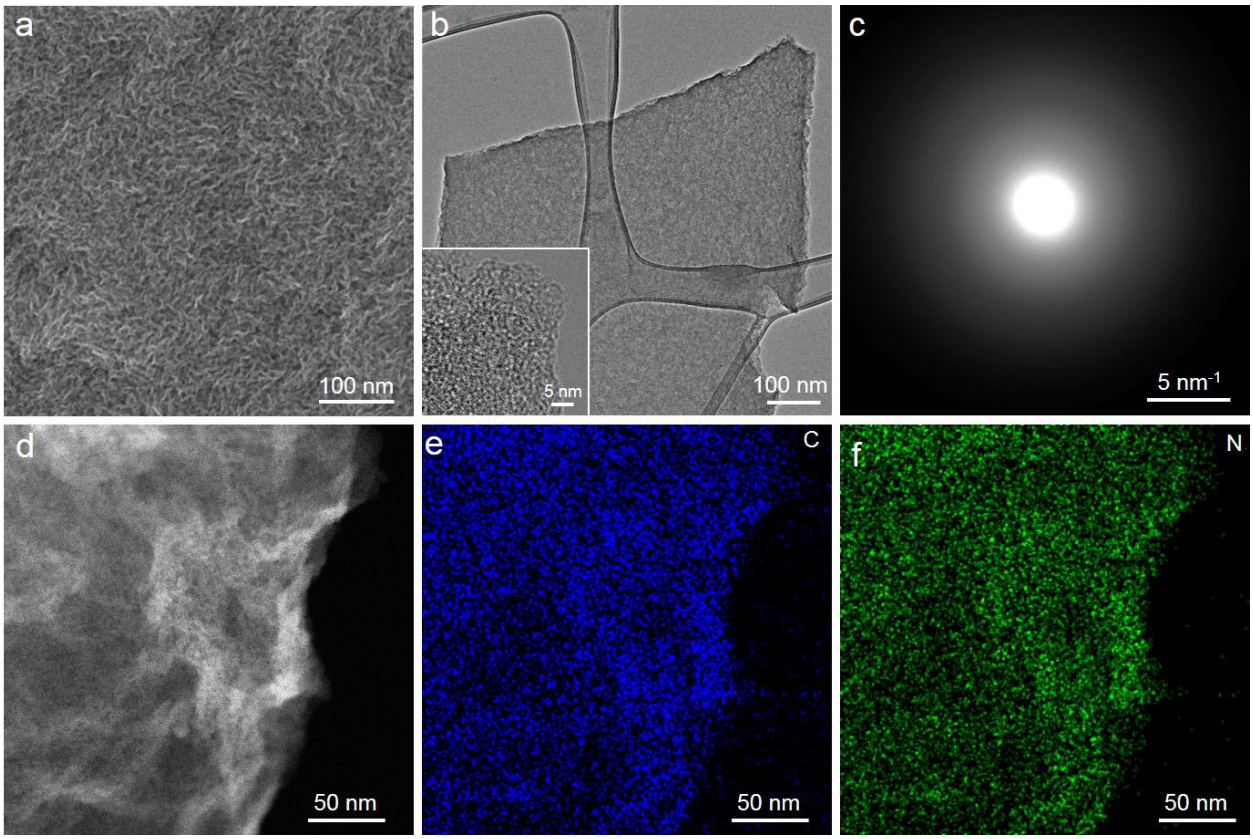

Figure S1. Additional characterization of the SA-Zn/MNC sample. (a) SEM image. (b) Low-magnification TEM image. The inset is its high-resolution TEM (HRTEM) image. (c) SAED pattern. (d) HAADF image, which is the same as the main panel in Figure 1a. (e) and (f) EDS mappings of C and N elements in the region of (d), respectively.

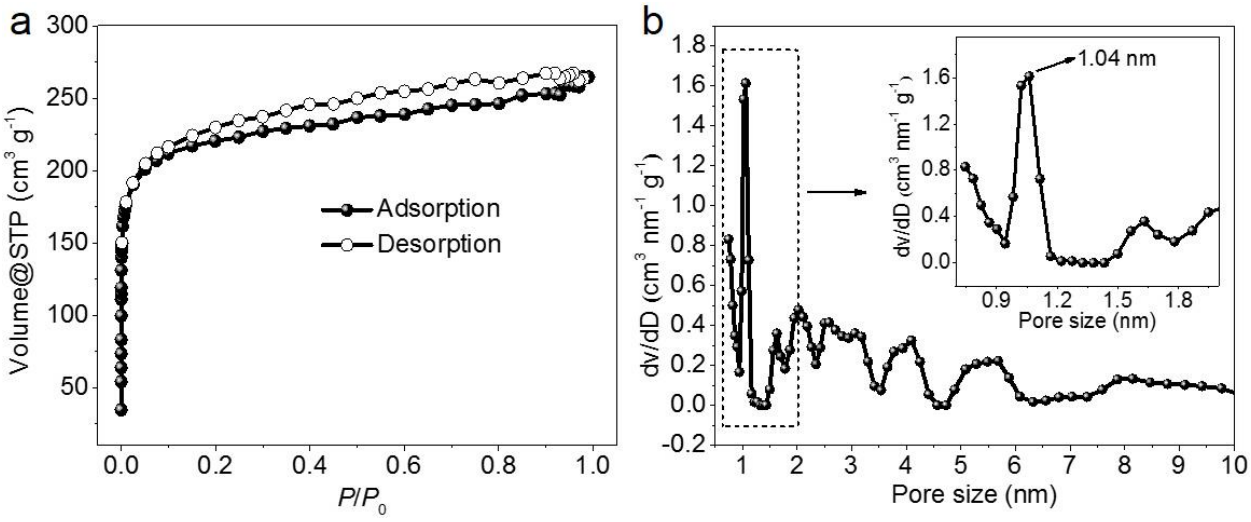

Figure S2. N_2 adsorption-desorption isotherms (a) and the corresponding pore size distribution (b) of SA-Zn/MNC. The inset in (b) is the enlargement of the boxed region in the main panel.

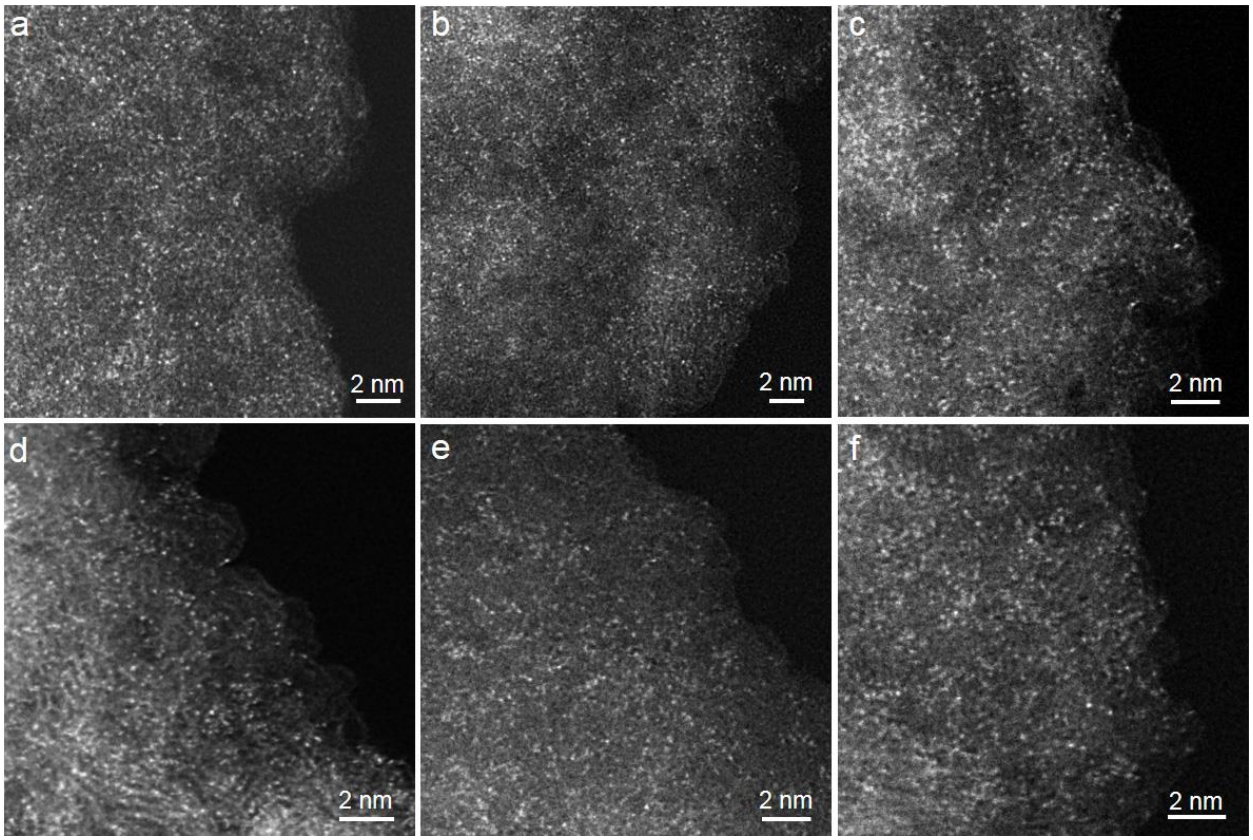

Figure S3. Additional atomic-resolution HAADF-STEM images of SA-Zn/MNC, showing that a plenty of Zn SAs are well dispersed over the sample. The images in (a-f) here and Figure 1b were taken on randomly selected regions in SA-Zn/MNC.

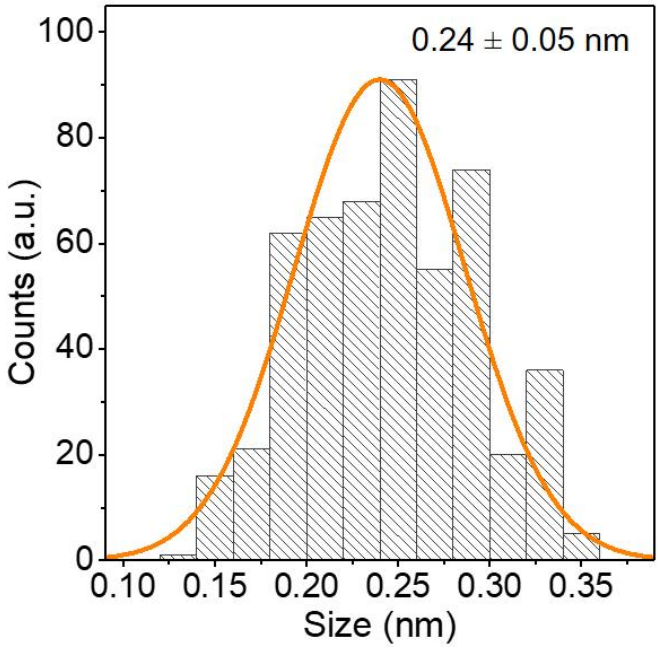

Figure S4. Atom size distribution graph obtained from atomic-resolution HAADF-STEM images in Figures 1b and S3. The average diameter is 0.24 ± 0.05 nm. The value is in an isolated atom size level (0.06 – 0.6 nm reported in https://en.wikipedia.org/wiki/Atomic_radius) and is close to the diameter of the Zn atom (0.278 nm reported in https://periodic.lanl.gov/30.shtml), convincing the existence of site-isolated Zn atoms.

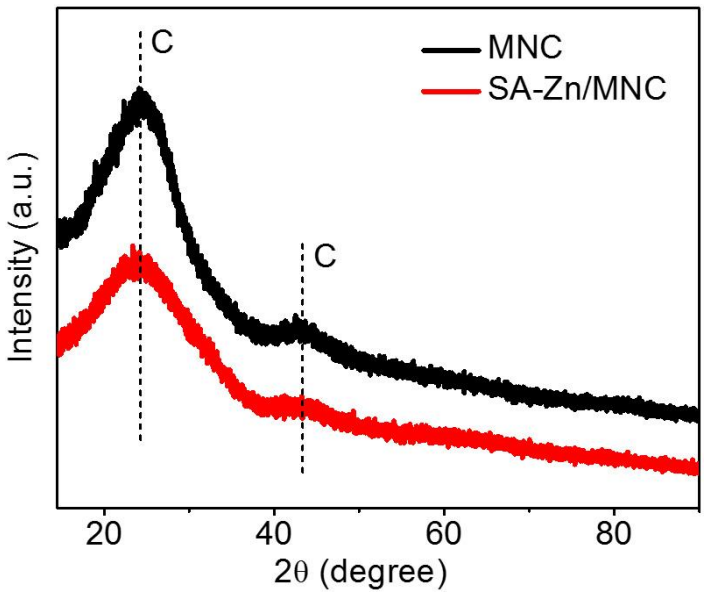

Figure S5. XRD patterns of MNC and SA-Zn/MNC, in which only carbon humps exist.

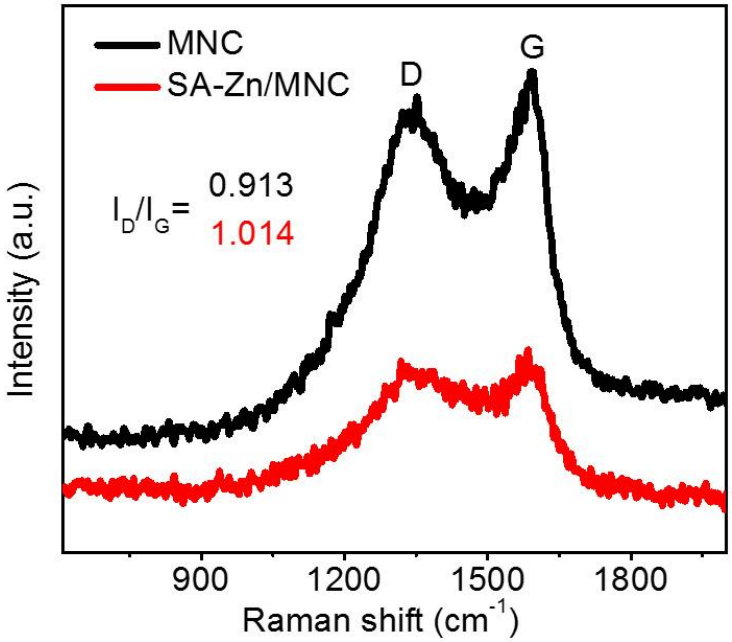

Figure S6. Raman spectra of MNC (black) and SA-Zn/MNC (red). The Raman spectra here show that, Compared with Zn-free MNC, SA-Zn/MNC has an increased I_D/I_G ratio, where I_D and I_G denote the intensity of the *D* and the *G* bands, respectively. Both *D* and *G* peaks derive from vibrations of sp^2-bonded carbon atoms. The *G* peak comes from in-plane vibrations of sp^2 bonded carbon atoms whereas the *D* peak is due to out of plane vibrations that attributed to the presence of structural defects (ref. 24). Therefore, the increased I_D/I_G ratio indicates that the doping of Zn into MNC induces more structural defects. This analysis is in good agreement with the existence of more micropores in SA-Zn/MNC, which is indicated by the lower SSA value of MNC (321 $m^2\ g^{-1}$).

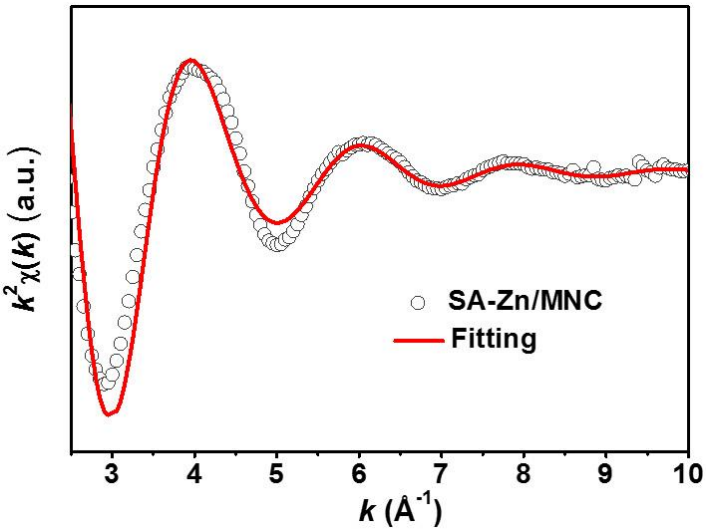

Figure S7. *k* space fitting curve with the Zn-N_4 configuration.

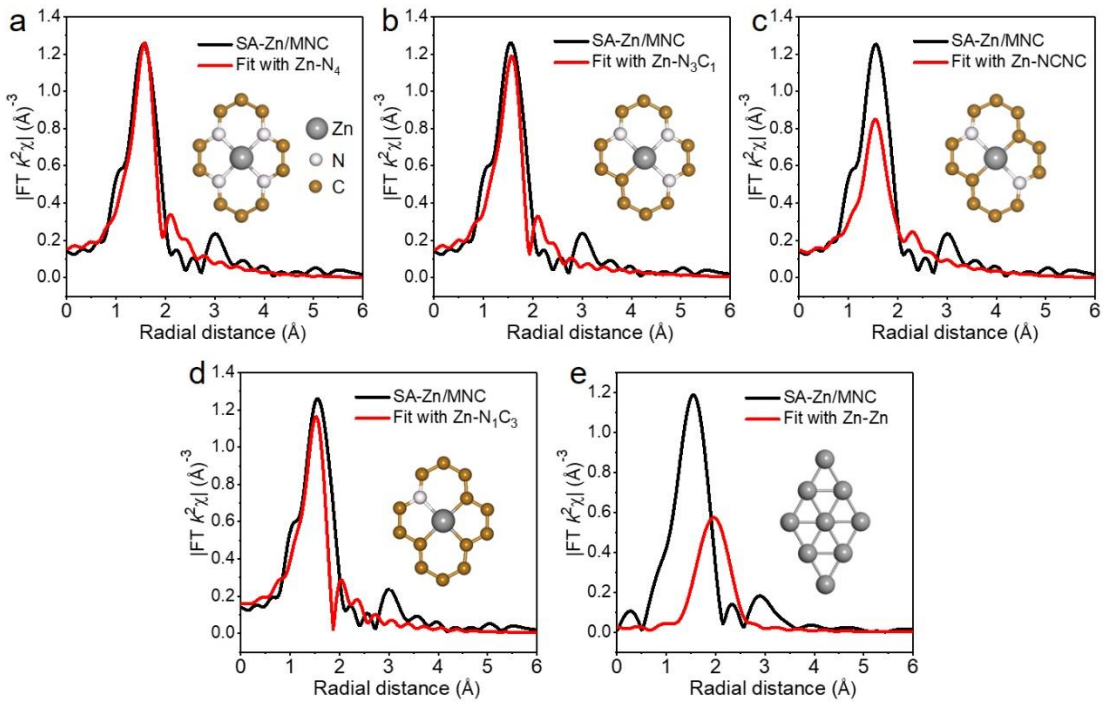

Figure S8. FT-EXAFS fittings of SA-Zn/MNC at Zn K-edge with Zn-N_4, Zn-N_3C_1, Zn-NCNC, Zn-N_1C_3 and Zn-Zn atomic models. (a) Zn-N_4 on graphene. (b) Zn-N_3C_1 on graphene. (c) Zn-NCNC on graphene, where the two nitrogen atoms are the opposite. Among all possible Zn-N_2C_2 models, the Zn-NCNC structure is calculated to be the most stable one from both energy and symmetry views. The inset is the atomic Zn-NCNC model. (d) Zn-N_1C_3 on graphene. (e) Zn-Zn coordination shell, which was generated using the metallic hexagonal close packing Zn crystal structure. Among Zn-N_4, Zn-N_3C_1, Zn-NCNC, Zn-N_1C_3 and Zn-Zn atomic structures, the Zn-N_4 model fits best with FT-EXAFS spectrum of SA-Zn/MNC (see more details in Table S1). This finding indicates that the Zn single atom is more likely atomically dispersed as Zn-N_4 on the support materials.

Table S1. Structural parameters of the SA-Zn/MNC sample obtained from the EXAFS fittings.

Structure	**Bond type**	***R* (Å)**	***CN***	**σ^2**	**E_0 shift (eV)**	**S_0^2**	***R*-factor**
Zn-N_4	Zn-N	2.05 ± 0.02	4.5 ± 0.8	0.006 ± 0.002	7.9	0.84	0.008
Zn-N_4*	Zn-N	2.03 ± 0.01	4	0.005 ± 0.001	6.71	1.00	0.09
Zn-N_3C*	Zn-N	2.00 ± 0.01	1	0.001 ± 0.001	3.47	1.00	0.12
	Zn-N	2.05 ± 0.01	2	0.001 ± 0.001	3.47	1.00	
	Zn-C	1.93 ± 0.01	1	0.001 ± 0.001	3.47	1.00	
Zn-NCNC*	Zn-N	2.16 ± 0.03	2	0.001 ± 0.001	6.62	1.00	0.169
	Zn-C	2.01 ± 0.04	2	0.001 ± 0.001	6.62	1.00	
Zn-N_1C_3*	Zn-N	2.0 ± 0.01	1	0.001 ± 0.001	0.1	1.00	0.26
	Zn-C	1.98 ± 0.01	2	0.004 ± 0.004	0.1	1.00	
	Zn-C	2.01 ± 0.01	1	0.004 ± 0.004	0.1	1.00	
Zn-Zn*	Zn-Zn	2.87 ± 0.2	6	0.028 ± 0.021	14.56	1.00	0.907

Note: *R*, the distance between absorber and backscatter atoms; *CN*, coordination number; σ^2, Debye–Waller factor; S_0^2, fitting from ZnO and defined as 0.84. The pretreatment of data was performed using Athena and the oscillation in the *k* range from 2.45 – 11.92 $Å^{-1}$ was selected for further EXAFS fitting. The EXAFS fitting of the Zn K edge spectrum was performed using Artemis.

* The coordination number is fixed during the fitting.

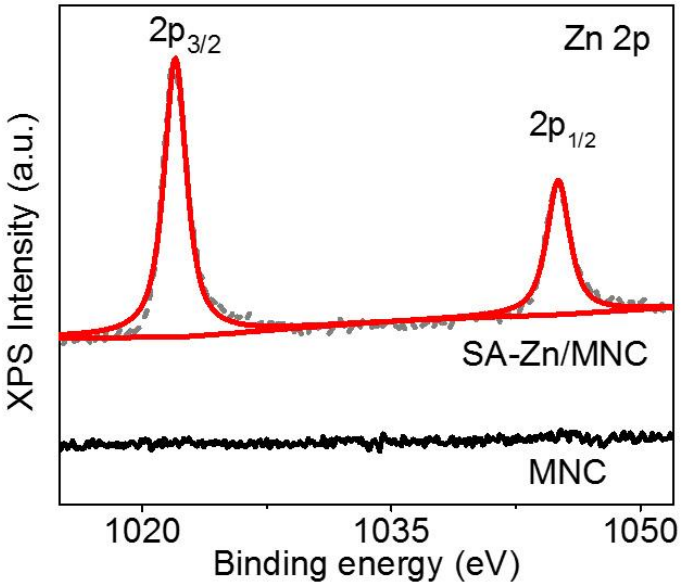

Figure S9. XPS peaks of SA-Zn/MNC (red) and MNC (black) for Zn 2p.

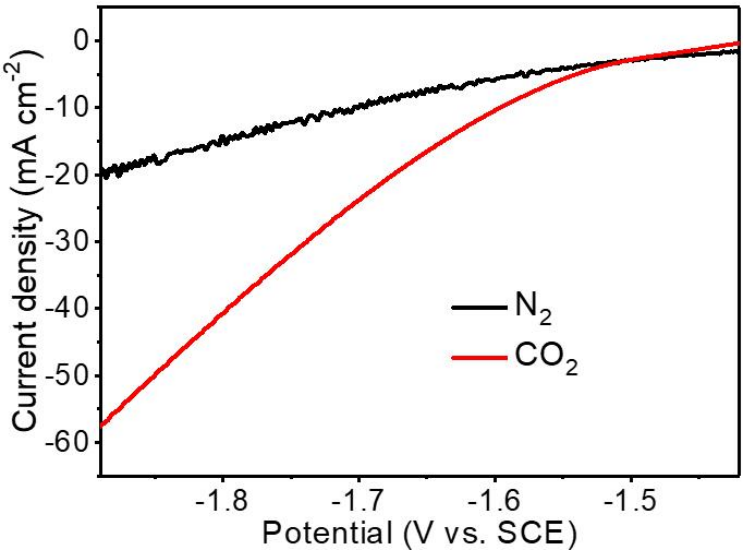

Figure S10. LSV curves of SA-Zn/MNC in N_2- and CO_2-saturated 1 M $KHCO_3$ with a scan rate of 10 mV s^{-1}. The red curve is the same as the red one in Figure 2a. In the N_2-saturated solution, the increase in the current at more negative potential was ascribed to the hydrogen evolution reaction (HER), which competes with the ERC. By contrast, SA-Zn/MNC provides a clearly increased reduction current in the CO_2-saturated electrolyte, suggesting that the reduction of CO_2 is catalytically more favorable relative to the HER.

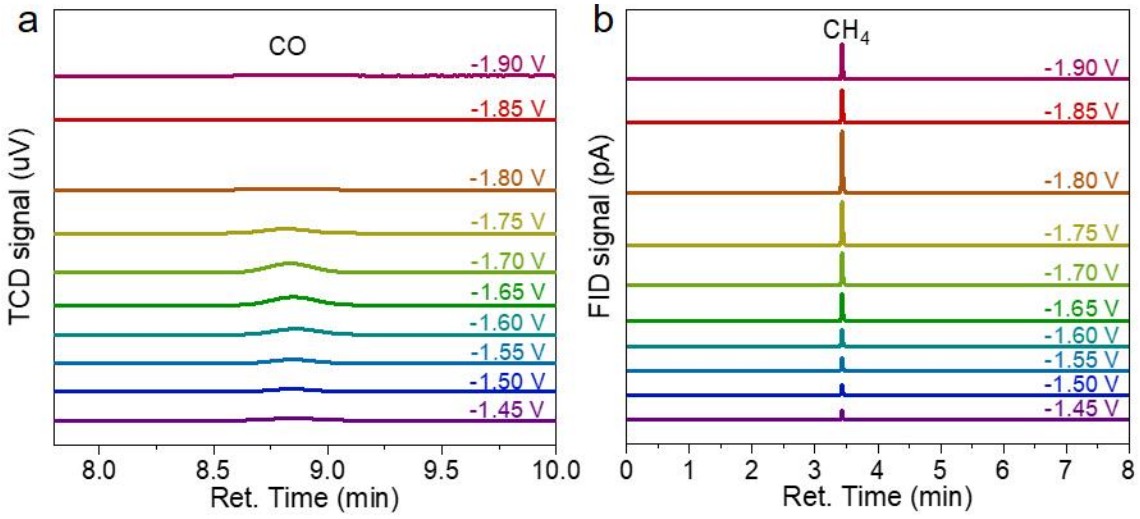

Figure S11. Gas chromatograph (GC) analyses of the generated products in the electrochemical reduction of CO_2 on the SA-Zn/MNC catalyst. (a) CO. (b)CH_4. By comparing the CO and the CH_4 GC spectra, it is found that the peak height of the CO spectrum at –1.8 V vs. SCE is far lower than those at –1.75 V, –1.7 V and –1.65 V vs. SCE, while the CH_4 one at –1.8 V vs. SCE reaches the maximum value. This comparison indicates that the CO production during ERC is suppressed at –1.8 V vs. SCE and instead

the CH_4 production is facilitated at –1.8 V vs. SCE. This result agrees well with that the FE for CH_4 production over the SA-Zn/MNC catalyst reaches its maximum value of 85% at –1.8 V vs. SCE in Figure 2b.

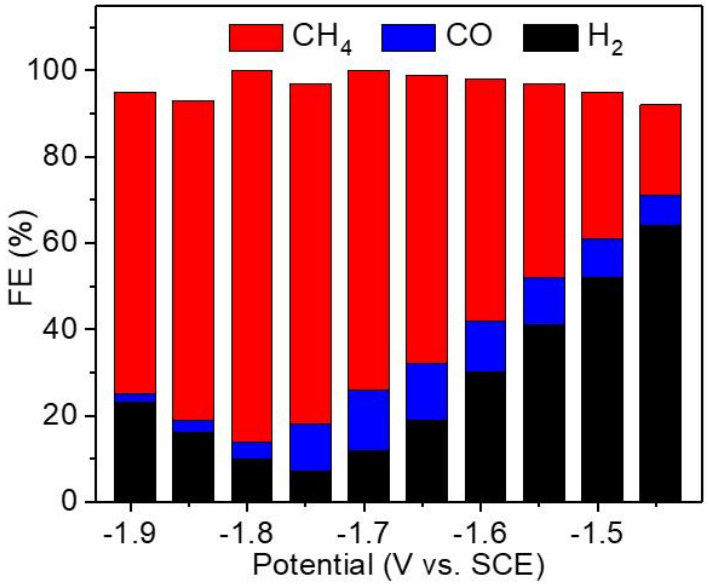

Figure S12. FE values of all ERC products and by-products on SA-Zn/MNC at different applied potentials.

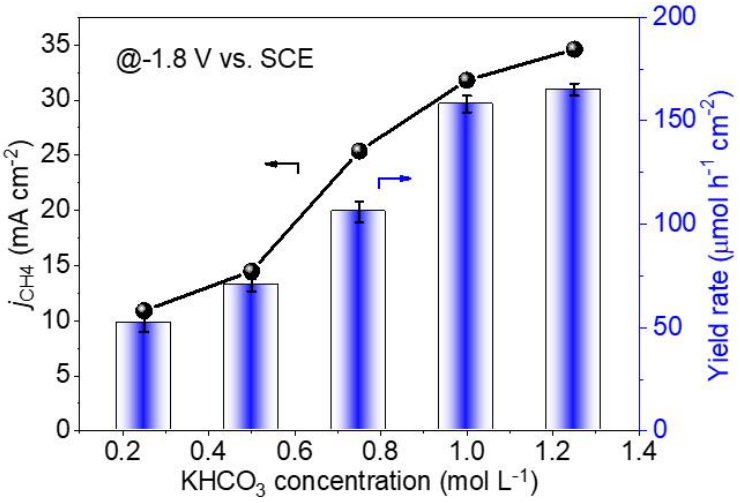

Figure S13. The partial current density and yield rate of CH_4 generated on SA-Zn/MNC electrode as functions of CO_2-saturated $KHCO_3$ concentration. Both the partial current density and the yield rate of CH_4 increase with $KHCO_3$ concentration. It can be explained by the correlation between electrolyte buffer capacity and local interfacial pH. (ref. 29) During ERC to CH_4, one CO_2 gets 8 protons to form one CH_4, so the partial current density of the reaction is proportional to proton activity. Higher $KHCO_3$ concentration increases the bulk pH, while their higher buffer capacity suppresses the increase of interfacial pH near the catalyst surface (local pH, pH_{local}) during the catalytic consumption of interfacial protons. Thus, the pH_{local} increased during ERC according pH_{local} (1.25 M $KHCO_3$) < pH_{local} (1 M $KHCO_3$) < pH_{local} (0.75 M $KHCO_3$) < pH_{local} (0.5 M $KHCO_3$) < pH_{local} (0.25 M $KHCO_3$), associated with the decrease of the local concentration of reactant protons, which explains the observed activity trends in Figure S13.

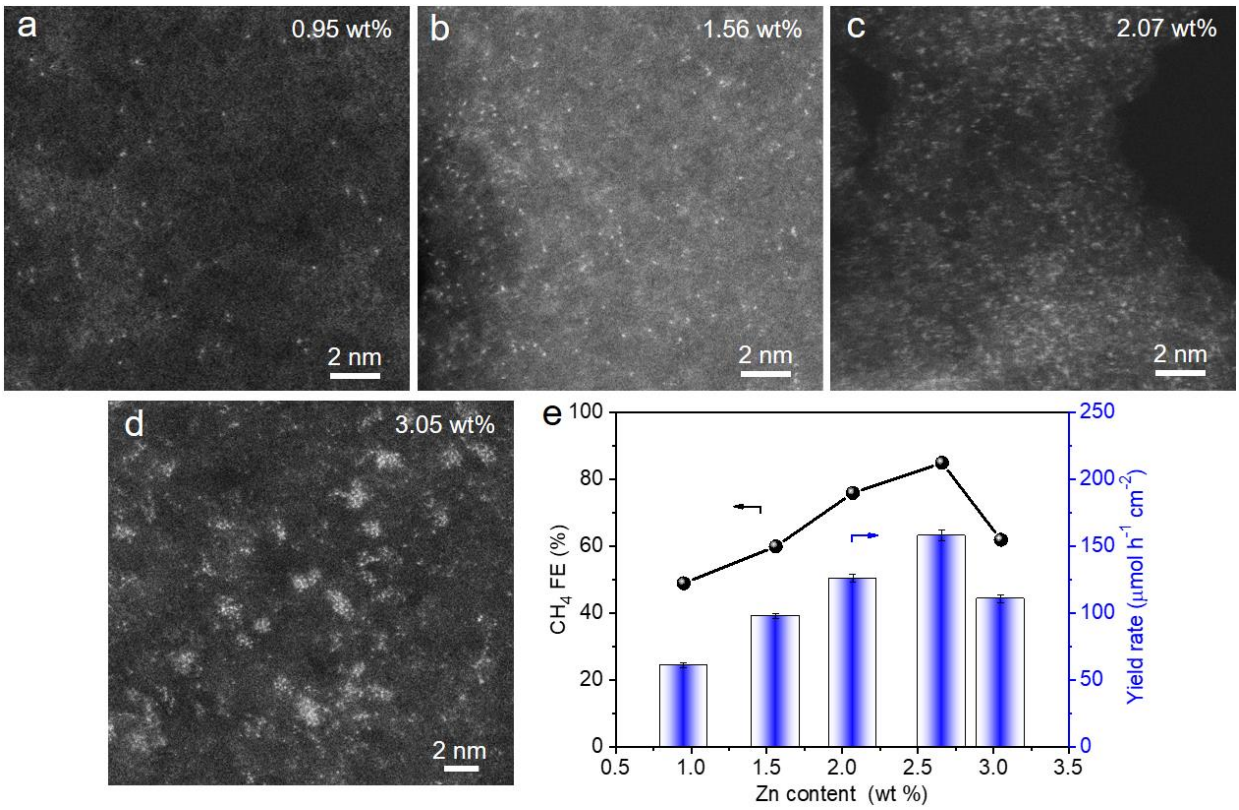

Figure S14. Relationship between Zn loading in SA-Zn/MNC and CH_4 production activity. (a-d) Atomic-resolution HAADF-STEM images with the Zn loadings 0.95 wt%, 1.56 wt%, 2.07 wt% and 3.05 wt%, respectively. Note: the atomic-resolution HAADF-STEM image with the Zn loading 2.66 wt% is shown in Figure 1b and Figure S3. (e) The FE and yield rate of CH_4 at –1.8 V vs. SCE as functions of Zn loading. From S14a-d, when the Zn content increases from 0 to 3.05 wt%, we have found that Zn nanoclusters appear at Zn loading of 3.05 wt%. From Figure S14e, it can be found that the FE and yield rate of CH_4 gradually improve with the Zn content and then decrease until the Zn content increases to 3.05 wt%. Increasing the Zn content, namely the density of the atomically dispersed active sites, can improve the activity. But when the Zn content is too large, Zn nanoclusters appear, which decreases the amount of the Zn-N sites and lower the activity. This finding indicates the core role of atomically dispersed Zn-N sites in the ERC electrocatalysis. Moreover, in Figure 2c, the CH_4 yield rate (158 ± 4 μmol h^{-1} cm^{-2}) of SA-Zn/MNC is 30 times more than that of MNC (5.24 ± 0.51 μmol h^{-1} cm^{-2}), meaning that 97% of CH_4 product is produced by the catalysis on Zn-related structure because MNC is Zn free. Additionally, according to previous studies[S9,S10], the pyridinic N is the active site for the reduction of CO_2 to CO. Since CO could weakly bond to the substrate, the further proton-electron transfer steps can hardly happen. Therefore, the CH_4 product is from N-Zn rather than P-N.

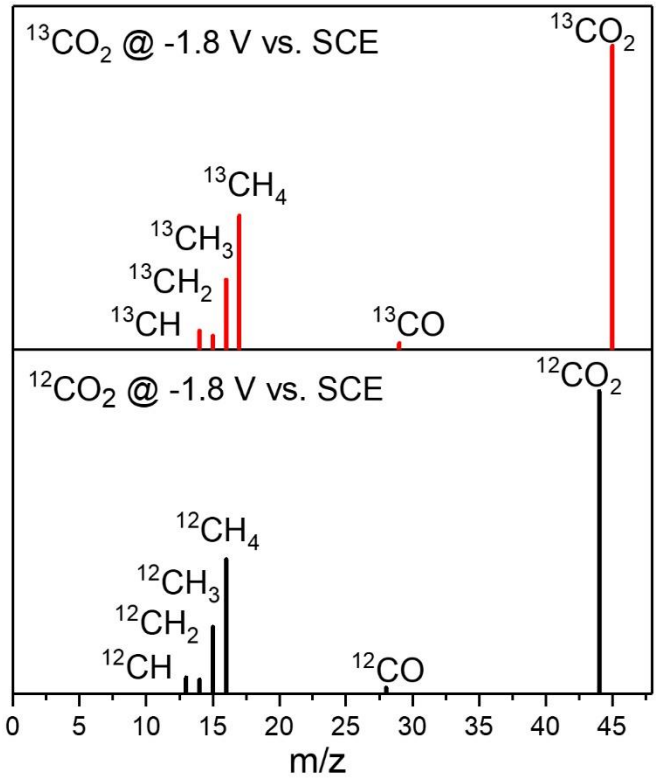

Figure S15. Mass spectra analyses of the CH_4/CO generated from $^{12}CO_2$ and $^{13}CO_2$ isotope electrochemical reduction experiments at –1.8 V vs. SCE on SA-Zn/MNC. In the ^{12}C spectrum, signals at m/z = 16, 15, 14, 13 are assigned to $^{12}CH_4$, $^{12}CH_3$, $^{12}CH_2$ and ^{12}CH, respectively, which result from $^{12}CH_4$ product. The weak signal at m/z = 28 is assigned to ^{12}CO product. Similarly, signals at m/z =17, 16, 15, 14 in the ^{13}C spectrum are associated with $^{13}CH_4$, $^{13}CH_3$, $^{13}CH_2$ and ^{13}CH from $^{13}CH_4$ respectively, and the weak signal at m/z = 29 is associated with ^{13}CO product (ref. 31). The results from the $^{13}CO_2$ isotopic-labeling and the $^{12}CO_2$ experiments clearly show that the ^{13}C-labeled CO_2 led to the formation of the predominant reduction product $^{13}CH_4$ accompanied by a trace amount of ^{13}CO, which is consistent with the results on $^{12}CO_2$. This is direct evidence that the evolved $^{13}CH_4$ originates solely from $^{13}CO_2$ gas.

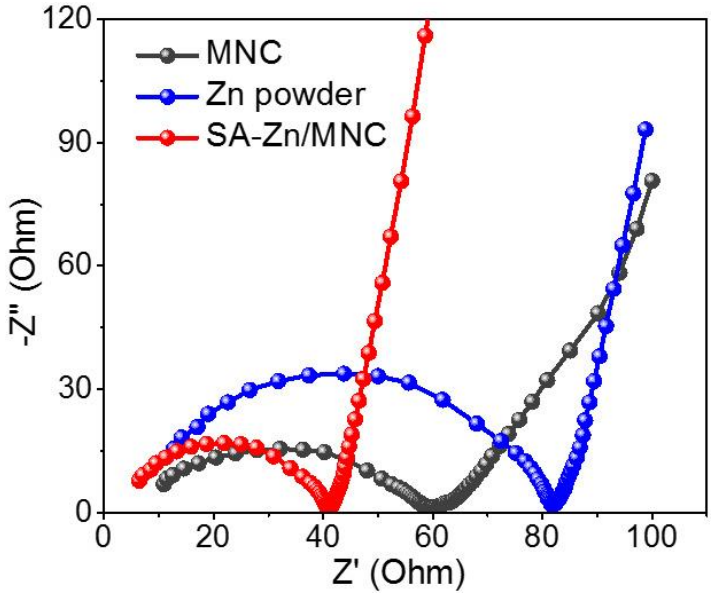

Figure S16. Nyquist plots of MNC, Zn powder and SA-Zn/MNC for EIS analysis. SA-Zn/MNC exhibited a lower interfacial transport resistance than MNC and Zn powder, suggesting faster charge transfer and reaction kinetics on SA-Zn/MNC (ref. 32).

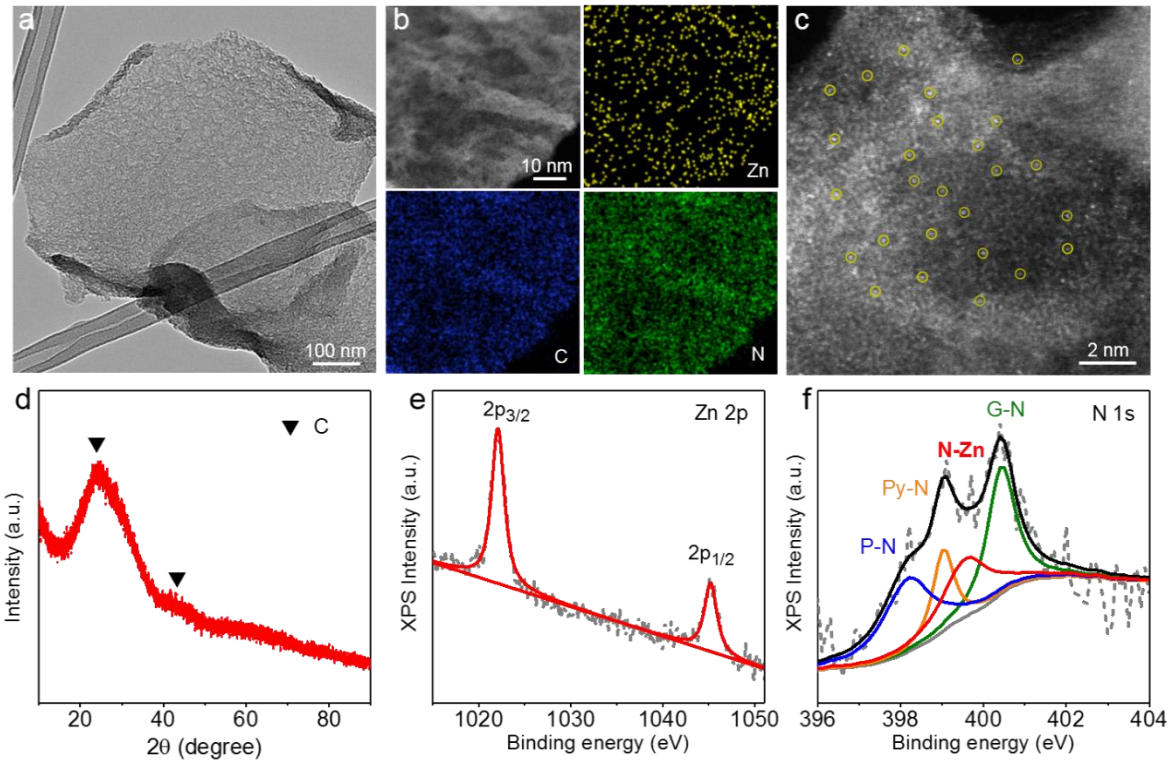

Figure S17. Characterization of the SA-Zn/MNC sample after the ERC electrochemical stability test. (a) TEM image. (b) HAADF image and EDS mappings of Zn, C and N elements in the same area. (c) Atomic-resolution HAADF-STEM image. (d) XRD pattern, in which only carbon humps exist. (e) Zn 2p XPS spectrum with peaks at 1022 and 1045 eV, which demonstrates that the Zn species keep +2 valence state. (f) N 1s XPS spectrum with pyridinic N (P-N), pyrrolic N (Py-N), N-Zn bonding and graphitic N (G-N) peaks, which suggests that the N-Zn bonding is still preserved in the SA-Zn/MNC sample. The results here were taken after the ERC-stability test. As shown in Figure S17a,b, the porous morphology is kept after the ERC process. The EDS mapping in Figure S17b displays the homogeneous dispersion of Zn on N-doped porous carbon. The atomic-resolution HAADF-STEM images in Figure S17c shows that the sample still keeps the atomic-dispersion property. The XRD pattern in Figure S17d shows that no Zn-related crystal peaks are observed. The XPS spectrum in Figure S17e exhibits that the Zn with XPS 2p peaks still at 1022 and 1045 eV keeps +2 state. The XPS analysis in Figure S17f demonstrates the existence of the Zn-N bonding still in SA-Zn/MNC. Moreover, ICP-OES analysis gives the Zn loading value to be 2.42 wt% after the ERC-stability test, very close to the value of 2.66 wt% before the ERC-stability test. These results demonstrate the stability of atomically dispersed Zn-N_4 during the ERC test, which agrees well with its catalytic property of the high stability for ERC to CH_4.

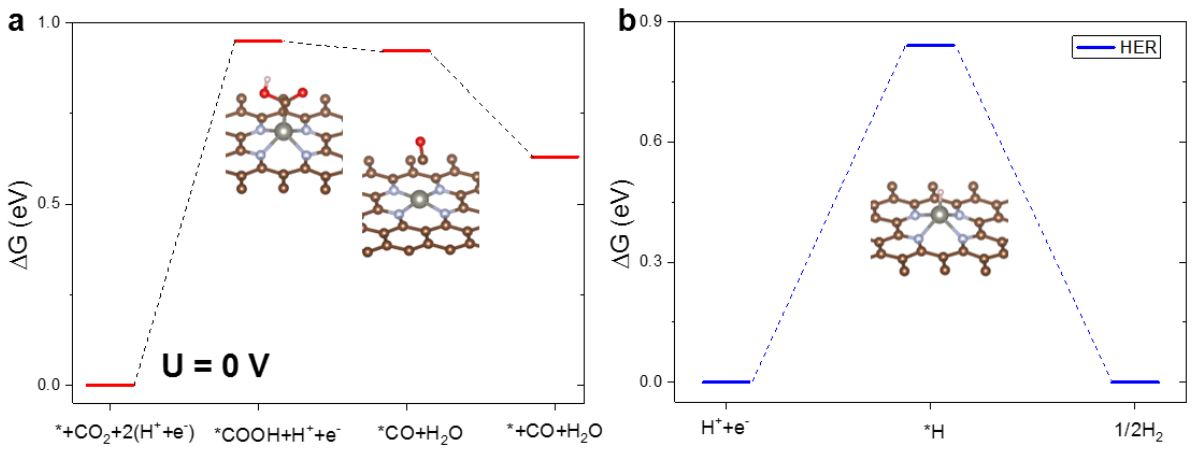

Figure S18. Free energy diagrams of (a) CO and (b) H_2 pathway for Zn-N_4-graphene. (a) The COOH step has a free energy barrier of 0.95 eV when the solvation correction is considered or 1.2 eV without the solvation correction. (b) The *H adsorption step has a free energy barrier of 0.84 eV. Compared with the free energy barrier of the *OCHO step (0.46 eV) in Figure 3a, both CO and H_2 formation are unfavorable. According to ref. 19, the CH_4 or CO favored pathway in DFT calculations depends on the first proton-electron transfer step, which is the formation of *OCHO (first step in CH_4 pathway) or *COOH (first step in CO pathway). Considering the reports for the Zn-N-C system in ERC (DFT calculation part specifically), either the *OCHO step has not been considered (refs 26 and 33), or the calculation model is in a finite system (ref. 26). To solve argument of the first protonation step, we considered both *OCHO and *COOH in our model. Based on our DFT calculations (Figure S18a,b), the *COOH formation has a 1.2 eV free energy barrier, compared with the 0.46 eV free energy barrier for *OCHO formation. Thus, the *OCHO formation is more favorable than the *COOH. As mentioned above, the *OCHO and the *COOH formations are for CH_4 and CO, respectively. Therefore, the favorable *OCHO formation blocks the next proton-electron transfer step to form CO. As a result, CH_4 is the final product with the free energy pathway shown in Figure 3a. For comparison, the free energy barrier for HER is 0.84 eV as shown in Figure S18b. This barrier comes from the first proton-electron transfer step. As a consequence, the higher barrier for adsorbed hydrogen than *OCHO formation further explains the high potential observed for current density reaching 10 mA cm^{-2} and the CH_4 as the main products other than H_2.

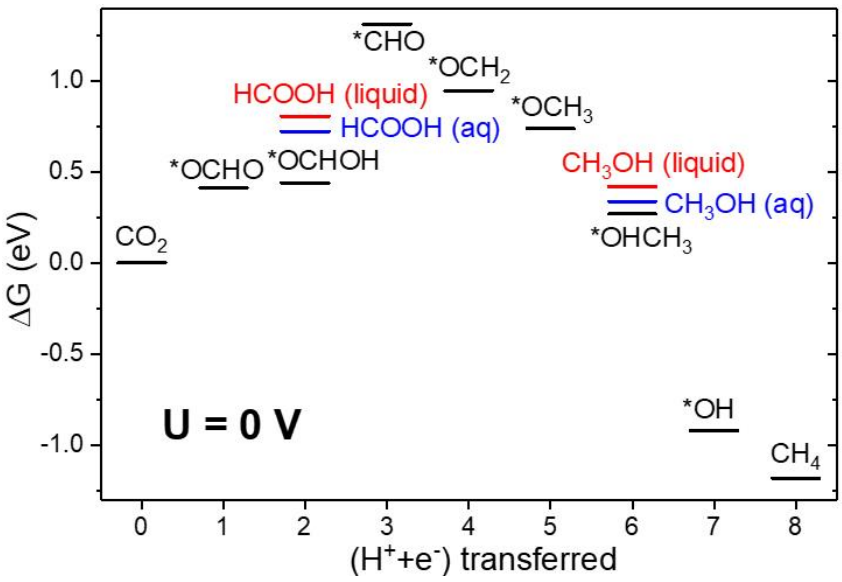

Figure S19. Free energy diagrams of ERC to CH_4 on Zn-N_4-graphene including HCOOH and CH_3OH liquid phase. The liquid phase free energy is estimated with calculated electronic energy and ZPE, while the entropy is from their liquid phase. The aqueous solution entropy of HCOOH and CH_3OH are estimated from the entropy change from the liquid phase to the aqueous phase. By considering the entropy change from the liquid phase where the concentration is 26.51 mol L^{-1} for HCOOH and 24.72 mol L^{-1} for CH_3OH to standard solution concentration, which is 1 mol L^{-1}, we estimated the entropy change as −0.084 eV for HCOOH and −0.082 eV for CH_3OH. *OCHOH has the same structure as HCOOH and is coordinated on the catalyst's surface by O. The result here shows that both *OCHOH and *$OHCH_3$ have lower free energies in adsorbed phases than the liquid phase. Therefore, formic acid and methanol are less likely to be desorbed as stable products. Desorption of $HCOO^-$ remains a possibility but is beyond our current consideration.

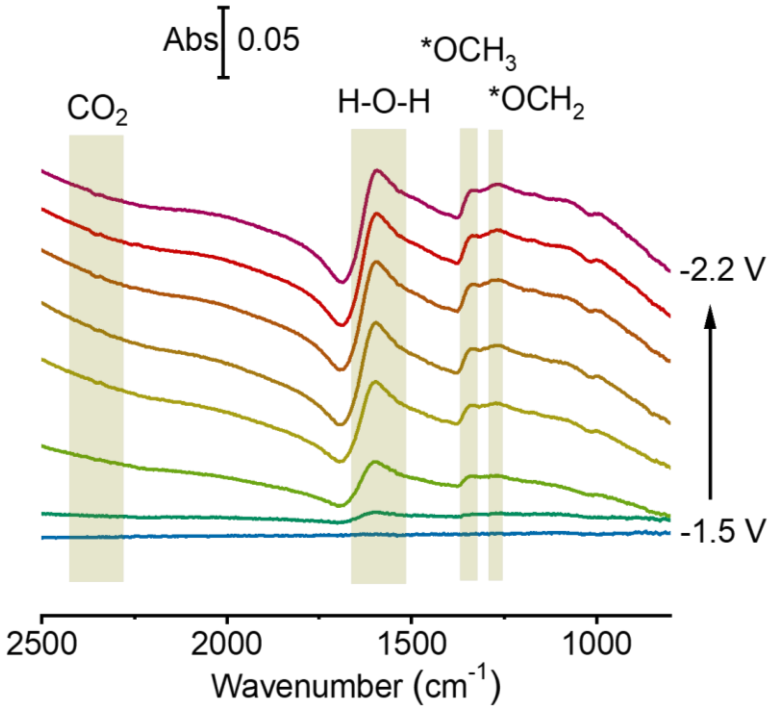

Figure S20. Operando ATR-SEIRAS measurements during ERC at the SA-Zn/MNC cathode at the different applied potentials in 1 M $KHCO_3$ purged with CO_2. The potentials are vs. SCE. The signal of CO_2 consumption in 1 M $KHCO_3$ aqueous electrolyte with applied potentials during the ERC is observed around 2350 cm^{-1} even though the signal is weak. The CO_2 concentration in the near-surface is quite stable even if the surface consumption rate is dynamic and high due to the CO_2-saturated concentrated $KHCO_3$ solution. ATR-SEIRAS are sensitive to relative changes, and therefore, the CO_2 band around 2350 cm^{-1} is weak. Moreover, there are no CO vibration peaks between 2100–1750 cm^{-1}, indicating that the generation of CO was suppressed during the ERC process (ref. 39). The upward bands at around 1338 and 1259 cm^{-1} could be, respectively, assigned to *OCH_3 (ref. 40) and *OCH_2 (ref. 41) with O coordinated on the catalyst's surface, which are consistent with the intermediates of CH_4 from the DFT calculation results in Figure 3.

Table S2. ERC-to-CH_4 results of this work and reported electrocatalysts in aqueous electrolyte solutions.

Catalyst	Electrolyte	FE_{max} (%)	J_{total} (mA cm^{-2})	*E* (V)	Time (h)	Ref.
Cu-based catalysts for producing CH_4						
Pulse electrodeposited Cu	0.5 M $NaHCO_3$	85	38	–2.8 (SCE)	Not Given (NG)	S11
		79	24	–2.5 (SCE)	NG	
		75	21	–2.3 (SCE)	1.2	
n-Cu/C	0.1 M $NaHCO_3$	80	13	–1.35 (RHE)	1	S12
CuS nanosheets	0.1 M $KHCO_3$	73 ± 5	7.3	–1.1 (RHE)	60	S13
Single-atomic Cu	0.1 M $KHCO_3$	58	60	−1.8 V (RHE)	2.2	S14
Cu NWs	0.1 M $KHCO_3$	55	~15	–1.25 (RHE)	NG	S15
Cu foil	0.1 M $KHCO_3$	57	23	–1.1 (RHE)	NG	S16
Polycrystalline copper	0.1 M $NaHCO_3$	50	4	–1.6 (Ag/AgCl)	1	S17
CuO_x NPs	0.1 M $KHCO_3$	~21	4	–1.0 (RHE)	6.7	S18
Cu/MoS_2	0.1 M $NaHCO_3$	17.1	~4	–1.4 (Ag/AgCl)	48	S19
Cu_2O films	0.1 M $KHCO_3$	9.85	14	–0.99 (Ag/AgCl)	NG	S20
Cu@GaN NW/Si	0.5 M $KHCO_3$	19	44.8	–1.4 (Ag/AgCl)	1.7	S21
Electrodeposited Cu	0.5 M KCl	26	~3	–1.2 (Ag/AgCl)	3	S22
Cu wafer	0.5 M $NaCO_3$	40	3	–1.0 (Ag/AgCl)	1	S23
Cu NPs	0.1 M $KHCO_3$	~20	15	–1.1 (RHE)	NG	S24
Cu Nanocube	0.1 M $KHCO_3$	56	-	–1.05 (RHE)	1	S25

Cu(II) phthalocyanine	0.5 M $KHCO_3$	66	13	–1.06 (RHE)	-	S26
Non-Cu-based catalysts for producing CH_4						
Ni_xGa_y alloys	0.1 M Na_2CO_3	2.1	120 uA	–0.88 (RHE)	NG	S27
Pd-Au	0.1 M KH_2PO_4/ 0.1 M K_2HPO_4	2	~15	–1.4 (RHE)	NG	S28
Ni stamp	0.5 M $KHCO_3$	~4	~5.25	–0.7 (SCE)	0.5	S29
Co protoporphyrin	0.1 M $HClO_4$	~2.5	~10	–0.8 (RHE)	NG	S30
S,N-doped polymer-derived carbon	0.1 M $KHCO_3$	0.18	~3	–0.99 (RHE)	27	S31
Wood-based activated carbons	0.1 M $KHCO_3$	1.2	1.4	–0.66 (RHE)	24	S32
Porous carbons	0.1 M $KHCO_3$	0.35	1.6	–1.0 (RHE)	6	S33
MNC	1 M $KHCO_3$	22	5.1	–1.8 (SCE)	NG	***This work***
Zn powder		0.92	9.6		NG	
SA-Zn/MNC		85	39.9		35	

Supporting References

S1. Miyake, H.; Ye, S.; Osawa, M., Electroless deposition of gold thin films on silicon for surface-enhanced infrared spectroelectrochemistry. *Electrochem. Commun.* **2002**, *4* (12), 973.

S2. Kresse, G.; Furthmüller, J., Efficient iterative schemes for ab initio total-energy calculations using a plane-wave basis set. *Phys. Rev. B* **1996**, *54*, 11169.

S3. Perdew, J. P.; Burke, K.; Ernzerhof, M., Generalized gradient approximation made simple. *Phys. Rev. Lett.* **1996,** *77*, 3865.

S4. Blöchl, P. E., Projector augmented-wave method. *Phys. Rev. B* **1994**, *50*, 17953.

S5. Peterson, A. A.; Abild-Pedersen, F.; Studt, F.; Rossmeisl, J.; Norskov, J. K., How copper catalyzes the electroreduction of carbon dioxide into hydrocarbon fuels. *Energy. Environ. Sci.* **2010**, *3*, 1311.

S6. https://webbook.nist.gov/

S7. Yang, F.; Song, P.; Liu, X.; Mei, B.; Xing, W.; Jiang, Z.; Gu, L.; Xu, W., Highly Efficient CO_2 Electroreduction on ZnN_4-based Single-Atom Catalyst. *Angew. Chem. Int. Ed.* **2018,** *57* (38), 12303.

S8. Gaussian 16, Revision C.01, Frisch, M. J.; Trucks, G. W.; Schlegel, H. B.; Scuseria, G. E.; Robb, M. A.; Cheeseman, J. R.; Scalmani, G.; Barone, V.; Petersson, G. A.; Nakatsuji, H.; Li, X.; Caricato, M.; Marenich, A. V.; Bloino, J.; Janesko, B. G.; Gomperts, R.; Mennucci, B.; Hratchian, H. P.; Ortiz, J. V.; Izmaylov, A. F.; Sonnenberg, J. L.; Williams-Young, D.; Ding, F.; Lipparini, F.; Egidi, F.; Goings, J.; Peng, B.; Petrone, A.; Henderson, T.; Ranasinghe, D.; Zakrzewski, V. G.; Gao, J.; Rega, N.; Zheng, G.; Liang, W.; Hada, M.; Ehara, M.; Toyota, K.; Fukuda, R.; Hasegawa, J.; Ishida, M.; Nakajima, T.; Honda, Y.; Kitao, O.; Nakai, H.; Vreven, T.; Throssell, K.; Montgomery, J. A., Jr.; Peralta, J. E.; Ogliaro, F.; Bearpark, M. J.; Heyd, J. J.; Brothers, E. N.; Kudin, K. N.; Staroverov, V. N.; Keith, T. A.; Kobayashi, R.; Normand, J.; Raghavachari, K.; Rendell, A. P.; Burant, J. C.; Iyengar, S. S.; Tomasi, J.; Cossi, M.; Millam, J. M.; Klene, M.; Adamo, C.; Cammi, R.; Ochterski, J. W.; Martin, R. L.; Morokuma, K.; Farkas, O.; Foresman, J. B.; Fox, D. J. Gaussian, Inc., Wallingford CT, **2016**.

S9 Sharma, P. P.; Wu, J.; Yadav, R. M.; Liu, M.; Wright, C. J.; Tiwary, C. S.; Yakobson, B. I.; Lou, J.; Ajayan, P. M.; Zhou, X.-D., Nitrogen-doped carbon nanotube arrays for high-efficiency electrochemical reduction of CO_2: On the understanding of defects, defect density, and selectivity. *Angew. Chem. Int. Ed.* **2015**, *54* (46), 13701.

S10 Jiang, Z.; Sun, H.; Wang, T.; Wang, B.; Wei, W.; Li, H.; Yuan, S.; An, T.; Zhao, H.; Yu, J.; Wong, P. K., Nature-based catalyst for visible-light-driven photocatalytic CO_2 reduction. *Energy. Environ. Sci.* **2018**, *11* (9), 2382.

S11. Qiu, Y.; Zhong, H.; Zhang, T.; Xu, W.; Li, X.-F.; Zhang, H., Copper electrode fabricated via pulse electrodeposition: toward high methane selectivity and activity for CO_2 electroreduction. *ACS Catal.* **2017**, *7*, 6302.

S12. Manthiram, K.; Beberwyck, B. J.; Alivisatos, A. P., Enhanced electrochemical methanation of carbon dioxide with a dispersible nanoscale copper catalyst. *J. Am. Chem. Soc.* **2014**, *136*, 13319.

S13. Zhao, Z.; Peng, X.; Liu, X.; Sun, X.; Shi, J.; Han, L.; Li, G.; Luo, J., Efficient and stable electroreduction of CO_2 to CH_4 on CuS nanosheet arrays. *J. Mater. Chem. A* **2017**, *5*, 20239.

S14. Wang, Y.; Chen, Z.; Han, P.; Du, Y.; Gu, Z.; Xu, X.; Zheng, G., Single-atomic Cu with multiple oxygen vacancies on ceria for electrocatalytic CO_2 reduction to CH_4. *ACS Catal.* **2018**, *8*, 7113.

S15. Li, Y.; Cui, F.; Ross, M. B.; Kim, D.; Sun, Y.; Yang, P., Structure-sensitive CO_2 electroreduction to hydrocarbons on ultrathin 5-fold twinned copper nanowires. *Nano Lett.* **2017**, *17*, 1312.

S16. Reske, R.; Mistry, H.; Behafarid, F.; Roldan Cuenya, B.; Strasser, P., Particle size effects in the catalytic electroreduction of CO_2 on Cu nanoparticles. *J. Am. Chem. Soc*. **2014**, *136*, 6978.

S17. Ahn, S. T.; Abu-Baker, I.; Palmore, G. T. R., Electroreduction of CO_2 on polycrystalline copper: Effect of temperature on product selectivity. *Catal. Today* **2017**, *288*, 24.

S18. Wang, X.; Varela, A. S.; Bergmann, A.; Kuhl, S.; Strasser, P., Catalyst particle density controls hydrocarbon product selectivity in CO_2 electroreduction on CuO_x . *ChemSusChem.* **2017**, *10*, 1.

S19. Shi, G.; Yu, L.; Ba, X.; Zhang, X.; Zhou, J.; Yu, Y., Copper nanoparticle interspersed MoS_2 nanoflowers with enhanced efficiency for CO_2 electrochemical reduction to fuel. *Dalton Trans.* **2017**, *46*, 10569.

S20. Ren, D.; Deng, Y.; Handoko, A. D.; Chen, C. S.; Malkhandi, S.; Yeo, B. S., Selective electrochemical reduction of carbon dioxide to ethylene and ethanol on copper(I) oxide catalysts. *ACS Catal*. **2015**, *5*, 2814.

S21. Wang, Y.; Fan, S.; AlOtaibi, B.; Wang, Y.; Li, L.; Mi, Z., A monolithically integrated gallium nitride nanowire/silicon solar cell photocathode for selective carbon dioxide reduction to methane. *Chem. Eur*. J. **2016**, *22*, 8809.

S22. Keerthiga, G.; Viswanathan, B.; Chetty, R., Electrochemical reduction of CO_2 on electrodeposited Cu electrodes crystalline phase sensitivity on selectivity. *Catal. Today* **2015**, *245*, 68.

S23. Dutta, A.; Rahaman, M.; Luedi, N. C.; Mohos, M.; Broekmann, P., Morphology matters: Tuning the product distribution of CO_2 electroreduction on oxide-derived Cu foam catalysts. *ACS Catal*. **2016**, *6*, 3804.

S24. Resasco, J.; Chen, L. D.; Clark, E.; Tsai, C.; Hahn, C.; Jaramillo, T. F.; Chan, K.; Bell, A. T., Promoter effects of alkali metal cations on the electrochemical reduction of carbon dioxide. *J. Am. Chem. Soc.* **2017**, *139*, 11277.

S25. Grosse, P.; Gao, D.; Scholten, F.; Sinev, I.; Mistry, H.; Roldan Cuenya, B., Dynamic changes in the structure, chemical state and catalytic selectivity of Cu nanocubes during CO_2 electroreduction: size and support effects. *Angew. Chem. Int. Ed.* **2018**, *57* (21), 6192-6197.

S26. Weng, Z.; Wu, Y.; Wang, M.; Jiang, J.; Yang, K.; Huo, S.; Wang, X. F.; Ma, Q.; Brudvig, G. W.; Batista, V. S.; Liang, Y.; Feng, Z.; Wang, H., Active sites of copper-complex catalytic materials for electrochemical carbon dioxide reduction. *Nat. Commun.* **2018**, *9*, 415.

S27. Torelli, D. A.; Francis, S. A.; Crompton, J. C.; Javier, A.; Thompson, J. R.; Brunschwig, B. S.; Soriaga, M. P.; Lewis, N. S., Nickel–gallium-catalyzed electrochemical reduction of CO_2 to highly reduced products at low overpotentials. *ACS Catal.* **2016**, *6*, 2100.

S28. Kortlever, R.; Peters, I.; Balemans, C.; Kas, R.; Kwon, Y.; Mul, G.; Koper, M. T. M., Palladium-gold catalyst for the electrochemical reduction of CO_2 to C-1-C-5 hydrocarbons. *Chem. Comm.* **2016**, *52*, 10229.

S29. Lan, Y. C.; Zhuge, W. Y.; Cui, D. H.; Cheng, X., Fabrication of nickel stamp using e-beam evaporation and electroforming for electroreduction of carbon dioxide. *J. Vac. Sci. Technol. B* **2017**, *35*, 2166.

S30. Shen, J.; Kortlever, R.; Kas, R.; Birdja, Y. Y.; Diaz-Morales, O.; Kwon, Y.; Ledezma-Yanez, I.; Schouten, K. J.; Mul, G.; Koper, M. T., Electrocatalytic reduction of carbon dioxide to carbon monoxide and methane at an immobilized cobalt protoporphyrin. *Nat. Commun*. **2015**, *6*, 8177.

S31. Li, W.; Seredych, M.; Rodriguez-Castellon, E.; Bandosz, T. J., Metal-free nanoporous carbon as a catalyst for electrochemical reduction of CO_2 to CO and CH_4. *ChemSusChem*. **2016**, *9*, 606.

S32. Li, W.; Herkt, B.; Seredych, M.; Bandosz, T. J., Pyridinic-N groups and ultramicropore nanoreactors enhance CO_2 electrochemical reduction on porous carbon catalysts. *Appl. Catal. B: Environ.* **2017**, *207*, 195.

S33. Li, W.; Fechler, N.; Bandosz, T. J., Chemically heterogeneous nitrogen sites of various reactivity in porous carbons provide high stability of CO_2 electroreduction catalysts. *Appl. Catal. B: Environ.* **2018**, *234*, 09263373.